International Journal of Mass Spectrometry 461 (2021) 116503

Contents lists available at ScienceDirect

International Journal of Mass Spectrometry

journal homepage: www.elsevier.com/locate/ijms

Tandem surface-induced dissociation of protein complexes on an ultrahigh resolution platform

Dalton T. Snyder [a], Yu-Fu Lin [a, b], Arpad Somogyi [a], Vicki H. Wysocki [a, b, *]

[a] Resource for Native MS Guided Structural Biology, The Ohio State University, Columbus, OH, 43210, USA
[b] Department of Chemistry and Biochemistry, The Ohio State University, Columbus, OH, 43210, USA

ARTICLE INFO

Article history:
Received 2 October 2020
Received in revised form
14 December 2020
Accepted 18 December 2020

Keywords:
Tandem surface-induced dissociation
Protein complex
FT-ICR
Ultrahigh resolution

ABSTRACT

We describe instrumentation for conducting tandem surface-induced dissociation (tSID) of native protein complexes on an ultrahigh resolution Fourier transform ion cyclotron resonance (FT-ICR) mass spectrometer. The two stages of SID are accomplished with split lenses replacing the entrance lenses of the quadrupole mass filter (stage 1, referred to herein as SID-Q) and the collision cell (stage 2, Q-SID). After SID-Q, the scattered projectile ions and subcomplexes formed in transit traverse the pre-filter prior to the mass-selecting quadrupole, providing preliminary insights into the SID fragmentation kinetics of noncovalent protein complexes. The isolated SID fragments (subcomplexes) are then fragmented by SID in the collision cell entrance lens (Q-SID), generating subcomplexes of subcomplexes. We show that the ultrahigh resolution of the FT-ICR can be used for deconvolving species overlapping in *m/z*, which are particularly prominent in tandem SID spectra due to the combination of symmetric charge partitioning and narrow product ion charge state distributions. Various protein complex topologies are explored, including homotetramers, homopentamers, a homohexamer, and a heterohexamer.

1. Introduction

Tandem mass spectrometry (MS/MS) is a workhorse for molecular structural elucidation, particularly in the fields of 'omics' (proteomics, metabolomics, lipidomics, etc.) and in the analysis of intact proteins and protein complexes [1–6]. 'Top-down' approaches [3,7–12] are commonly used to generate sequence fragments from denatured or otherwise restructured proteins, providing a direct measurement of primary structure. Collision induced dissociation (CID), electron transfer dissociation (ETD) [2,8,8,13], electron capture dissociation (ECD) [14–17], ultraviolet photodissociation (UVPD) [7,10,11,18], and infrared multiphoton dissociation (IRMPD) [19–22] are the most commonly employed top-down MS/MS techniques and are widely available on commercial platforms or can be implemented in existing instruments by third party vendors. Native proteins and protein complexes can also be studied by ETD [13,23], ECD [12,24], UVPD [12,25–28], and IRMPD [19], though the typically folded and more compact structures of native ions makes dissociation more difficult because fewer residues are surface-exposed. Nonetheless, sequence fragments and even subcomplexes (in some cases) can be generated from native protein complexes using these techniques; sequence fragments usually originate from solvent-accessible residues, thus providing a glimpse into tertiary and quaternary structure but providing insufficient information for deducing the connectivity within multi-subunit protein complexes. Surface-induced dissociation (SID) [29] can be used for top-down protein analysis by producing b- and y-type fragment ions [30–33] similar to those produced by the more commonly employed CID, or SID can be employed for complex-up/complex-down analysis of protein complexes. The CID technique is widely available on commercial platforms, whereas SID commercialization is only beginning to emerge at the time of this writing (e.g. on Waters' SELECT SERIES Cyclic IMS [34]), in part due to recent simplification of SID ion optics [35].

The obvious utility of SID for mass spectrometry is its ability to produce compact, topologically-consistent subcomplex fragments from noncovalent protein complexes [36–39], a feature not shared with other activation techniques. When subjected to a surface collision, protein complexes dissociate in a manner consistent with their assembly and subunit connectivity, with the smallest and weakest intersubunit interfaces preferentially breaking at low

* Corresponding author. Resource for Native MS Guided Structural Biology, The Ohio State University, Columbus, OH, 43210, USA.
E-mail address: wysocki.11@osu.edu (V.H. Wysocki).

https://doi.org/10.1016/j.ijms.2020.116503
1387-3806/

collision energy [40,41] while retaining noncovalent interactions within the subcomplex fragments, although ion mobility measurements suggest that some gas-phase restructuring can occur in activated, but not dissociated, precursors as well as subcomplex fragments [38]. Subunit-ligand interactions can be probed by SID [42], depending on the binding interactions between the ligand and subunit. The unique noncovalent fragmentation patterns are useful for partially reconstructing protein complex structure without cryo-EM or x-ray diffraction data or as a complementary structural biology technique [43–45].

Multiple stages of dissociation (MS^n) [46] are a useful tool for structural biology studies of proteins and protein complexes [47], particularly if those MS/MS stages involve an intermediate stage of mass selection to increase analytical selectivity. MS^n, or pseudo-MS^n if *m/z* or mobility selection are not available for each activation stage, allows additional structural information to be obtained from large species. A ligand-bound protein complex, for example, may first be dissociated into subcomplexes and then further into monomers or sequence fragments in order to deduce the location and interactions of the ligand with the protein (depending on the type of binding between the ligand and protein – some are more easily lost [9,26]).

There are several studies that have combined collisional, electron-based, and/or photon-based activation methods for improving sequence coverage [12,16,48–55], but few have demonstrated consecutive fragmentation of mass-selected ions and even fewer have addressed consecutive dissociation stages of protein complexes. The Robinson group has demonstrated dissociation of protein complexes into subcomplexes and then into components on an Orbitrap tribrid system in order to identify bound ligands [47]. The Kelleher group demonstrated a pseudo-MS^3 approach on an Orbitrap platform, dissociating 14mer GroEL into a monomer (and complementary 13mer) through in-source dissociation and subsequently into sequence fragments by higher energy collisional activation in the HCD cell [56]. The Kelleher group then described an MS^n approach for characterizing endogenous protein complexes by native MS combined with 'omics' MS/MS techniques [47]. The Brodbelt group demonstrated the mapping of phosphate locations on lipid A using an MS^3 strategy with CID and UVPD for successive fragmentation [57]. The group also used in-source CID to produce monomers from the homodimer of human mitochondrial enzyme branched-chain amino acid transferase 2 (BCAT2) and subsequently generated sequence fragments from the monomers by UVPD [58]. The Sharon lab utilized a triple-stage mass spectrometry experiment on a hybrid Orbitrap platform to elucidate the heterogeneity of the yeast homotetrameric FBP_1 complex by mapping distinct phosphorylation sites on the protein in response to glucose supplementation and heat shock treatment, which was not possible with the conventional MS^1 or MS^2 experiments [59]. These studies highlight the need for more robust consecutive fragmentation methods for probing protein-ligand interactions, where ligand can be a small molecule or another biological macromolecule such as protein, RNA, or DNA, and for increasing topological and sequence coverage from single MS^n experiments, preferably on high-resolution platforms.

In a similar manner, our group has previously reported tandem SID (SID/SID, or tSID) of noncovalent protein complexes on a low-resolution Q-IM-TOF platform [60]. A 10-lens SID device was placed at the entrance and exit of a travelling wave ion mobility cell. Mass-selected protein complexes were fragmented by a first stage of SID, the fragments were separated in the mobility cell (allowing fragmentation of mobility-separated species), and a second stage of dissociation (CID or SID) was used to further characterize the assembly of several model complexes. This tSID methodology was useful for probing the quaternary structure of toyocamycin nitrile hydratase, a heterohexamer for which there is no high-resolution crystal structure [37]. Tandem SID experiments provided key topological information which, when combined with covalent labeling and solution disruption experiments, resulted in the first proposed model for the protein's subunit connectivity [43]. This experiment highlighted the advantages of a tandem SID configuration for successively fragmenting protein complexes of unique topologies. Unfortunately, it has remained difficult to translate this tSID implementation to other platforms due to the size of the 10-lens SID device, requiring ~3 cm along the ion path axis for each device. Removal of a total of 6 cm of ion optics in many commercial platforms is not viable without compromises to sensitivity or instrument functionality.

Here we describe a miniature tSID configuration (3 mm for each device) on an ultrahigh resolution FT-ICR platform and use it to successively fragment several model noncovalent protein complexes. This is the first demonstration of tandem SID on an ultrahigh resolution platform, but more importantly this arrangement allows an estimate of the dissociation time frame for large protein complexes after a surface collision, a timing determined by the distance traveled from the first surface to the entrance of the quadrupole (about 20–30 μsec for the complexes investigated here).

2. Experimental

2.1. Chemicals

Ammonium acetate, triethylammonium acetate (TEAA), ethylenediamine diacetate (EDDA), cesium iodide, streptavidin, cholera toxin B (CTB), and concanavalin A (ConA) were obtained from Sigma-Aldrich (St. Louis, MO). C-reactive protein (CRP) was purchased from Lee Biosolutions (Maryland Heights, MO, USA). HFQ65 was obtained from the Woodson group at Johns Hopkins University. His-tagged and untagged toyocamycin nitrile hydratase (TNH) were obtained from the Bandarian laboratory at the University of Utah [61]. Protein complexes were buffer exchanged twice into 200 mM ammonium acetate using 6 kDa cutoff size exclusion chromatography spin columns (Bio-Rad). Typical concentrations used for these studies were in the range of 5–10 μM of protein complex after charge reduction. TEAA and EDDA were added to protein standards as charge reducing agents for a final concentration of 60 mM reducing agent and 140 mM ammonium acetate. Mass and quadrupole calibration up to *m/z* 8000 were accomplished using 10 mM cesium iodide as a standard. Typical mass errors after calibration were <1.5 ppm throughout the mass range, with typical errors <300 ppb below *m/z* 2000.

2.2. Ionization

Gas-phase protein ions were generated by nanoelectrospray ionization using borosilicate capillary emitters with ~1–2 μm tip diameter. These were prepared in-house using a Sutter Instrument P-97 tip puller (Novato, CA). Spray voltage, applied to the inlet capillary of the instrument, was typically 1 kV or less.

2.3. Instrumentation

Tandem SID was conducted on a Bruker solariX XR 15 T FT-ICR mass spectrometer equipped with a nanoelectrospray ionization source (Fig. 1). The quadrupole rf driver was modified (by KapScience, LLC, Tewksbury, MA) from an original 880 kHz model to have an operating frequency of 343 kHz, permitting mass selection of ions up to *m/z* 30,000. All rf-only devices, including the source funnels, source octupole, and collision cell, were set to their highest

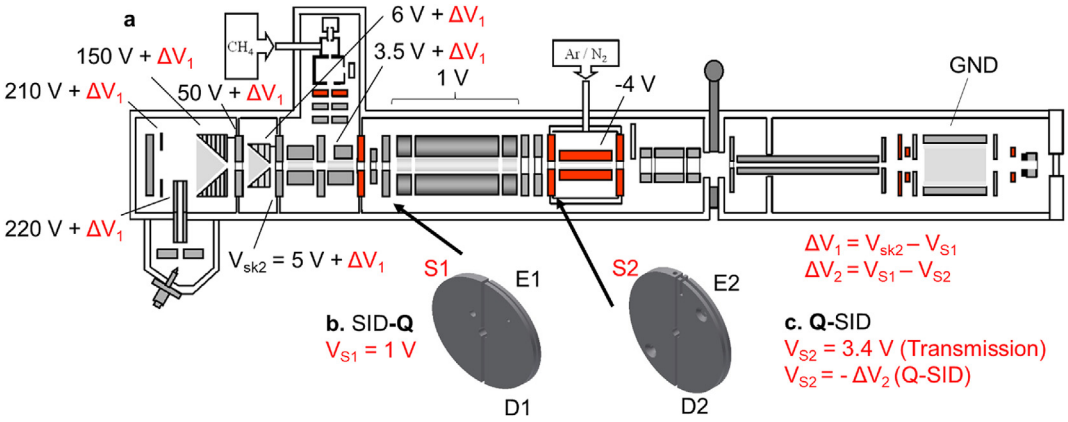

Fig. 1. Tandem surface-induced dissociation of protein complexes on an ultrahigh resolution FT-ICR. (a) Instrument diagram showing an electrospray ionization source, two ion funnels and skimmers, a transport octupole, a mass-selecting quadrupole, and a collision cell with entrance and exit lenses (red) for CID and for ion accumulation. After accumulation, the ions are pulsed from the collision cell into the FT-ICR cell on the right. (b) The entrance lens of the quadrupole has been modified with a double split lens for SID, termed **SID-Q**, and (c) similarly the entrance lens of the collision cell has been modified for SID, termed **Q-SID**. While the three Q-SID lenses can be operated independently, the SID-Q surface and extractor are electrically connected for convenience. S = surface, D = deflector, E = extractor. The SID-Q collision voltage (ΔV_1) is the difference between the skimmer 2 voltage (V_{sk2}) and the first surface (S1) voltage, and the Q-SID collision voltage (ΔV_2) is the potential difference between S1 and the second surface (S2). (For interpretation of the references to colour in this figure legend, the reader is referred to the Web version of this article.)

rf voltages and lowest frequencies, aside from the transport multipole between the collision cell and the FT-ICR cell, which was set at 2 MHz and 450 V_{pp}. The collision cell was filled with argon for collisional cooling and CID. Our FT-ICR also has modified source funnels that allow for trapped ion mobility spectrometry (TIMS) experiments to be accomplished, though this technique was not used here and is still being evaluated in-house in conjunction with SID. Mass spectra were acquired as an average of 10–20 scans covering a mass range of *m/z* 1000 to *m/z* 20,000, 1 M transient length (~2.3 s), and time-of-flight in the range of 1.5–2 ms, depending on the *m/z* range of the analyte ions. For single stage SID experiments, accumulation times were ~1s or less, whereas for multi-stage SID/SID experiments accumulation times ranged from 2 to 40 s, depending on the absolute scattering yield of the first stage of SID and the efficiency of quadrupole isolation after SID. The increased accumulation time is needed to produce sufficient S/N after two stages of dissociation in which there is signal loss in each stage. Although the SID product ion collection efficiency (SID signal as percentage of transmission signal) in the entrance lens of the collision cell (Q-SID) is 20–30% as characterized previously [35], we expect the pre-quadrupole (SID-Q) efficiency to be lower for several reasons. First, the quadrupole has worse ion beam acceptance than the hexapole collision cell, and we are diverting the ion beam off axis and bringing it back on axis in the quadrupole pre-filter to accomplish SID-Q, which should result in rejection of a portion of the ion beam. Second, due to mass-selective stability/instability, more ion losses are observed in rf/dc mode than when operating the quadrupole in rf-only mode, whereas the collision cell is always operated in rf-only mode. Despite the potential signal losses, we placed the first SID device in the entrance lens of the quadrupole for several reasons: 1) it is more accessible than the source optics, 2) it is maintained at a pressure of $<1 \times 10^{-5}$ mbar (whereas the preceding chambers are at higher pressure), and 3) it permitted the acquisition of stopping curves of SID product ions by varying the post-filter voltage, as described later.

To accomplish the two consecutive stages of SID, the entrance lenses of the quadrupole mass filter and collision cell were each replaced with a 'Gen 3' split lens comprising a deflector (D), a surface (S), and an extractor (E) (Fig. 1b and c) [35]. All SID lenses are polished stainless steel but are otherwise untreated and are not coated with self-assembled monolayers. In general, the metal surfaces in the Gen 3 device are cleaned approximately every 2 months after 2–3 days/week of SID work. Through application of a repulsive dc voltage, the deflector guides ions into the untreated (but cleaned and polished) stainless steel surface, which is held at an attractive potential commensurate with the SID energy of interest. (Note that the surface is likely coated with adventitious hydrocarbons as is typical for metal surfaces in vacuum at normal mass spectrometry pressures.) The ions collide with the surface and are transmitted into either the rf-only quadrupole pre-filter (SID-Q) or the rf-only hexapole collision cell (Q-SID). Throughout this manuscript, when we discuss SID in the entrance lens of the quadrupole, we use the terminology *SID-Q* (i.e. SID prior to the quadrupole, collision with S1), whereas for SID in the entrance lens of the collision cell, we use the term *Q-SID* (i.e. SID after the quadrupole, collision with S2). While both SID-Q and Q-SID devices are composed of three electrodes, the surface and extractor of the SID-Q device are electrically connected for convenience while they remain independent for Q-SID. Thus, there are two independent potentials for SID-Q (deflector and surface/extractor) and three for Q-SID (deflector, surface, and extractor), for a total of five tunable voltages during tSID. Typical voltages applied in the source region during transmission are given in Fig. 1. Please note that the effective birth potential of the ions under these conditions is approximately equivalent to the skimmer 2 voltage (V_{sk2}).

To conduct SID-Q, all ion optics up to the first surface (S1) are increased in voltage (ΔV_1 in Fig. 1) relative to the first surface while the deflector is tuned 40–60 V more positive than the surface, which is held at 1 V. The quadrupole pre-filter voltage was optimized for SID-Q signal intensity for each protein complex, but in general was held 5–15 V lower than the first surface and did not alter relative abundances of product ions. The kinetic energy of the ions in the FT-ICR is set initially by the voltage on skimmer 2, as determined by simple stopping curves [62], and so the SID-Q collision energy is defined as the difference in voltage between the skimmer 2 and the SID-Q surface multiplied by the ion charge state. The internal power supply for the skimmer is limited to 100 V, and so we are limited to 100 V for the first stage of SID.

After precursor collision with the surface of the first SID device, the newly formed fragment ions as well as unfragmented precursor ions are passed through the rf-only prefilter and may then be mass-selected in the rf/dc quadrupole. The mass-selected precursor or

fragment ions are then subjected to a second stage of SID in the entrance lens of the collision cell (tSID, or SID-Q-SID), collected in the collision cell for transfer to the ICR cell, or fragmented by CID (SID-Q-CID) in the collision cell.

Q-SID is accomplished by dropping the Q-SID surface voltage from its usual 3.4 V bias during transmission mode to a desired negative voltage ($-\Delta V_2$) while simultaneously dropping the DC offset on the collision cell rods to be more attractive than the surface so that ions collide with the surface and are then collected in the collision cell. The Q-SID deflector and extractor are tuned to maximize SID sensitivity while simultaneously avoiding accidental CID contamination (by missing the surface). The difference in voltage between the SID-Q surface and the Q-SID surface ($-\Delta V_2$) multiplied by the ion charge state determines the Q-SID collision energy in the tSID experiment. Strictly speaking, this ignores any residual kinetic energy from the SID-Q collision, which is not known but is estimated as 10%–20% based on comparisons to SIMION simulations and preliminary results reported here. Because the internal power supplies for the surface and collision cell are limited to ± 100 V, the second stage of SID is also limited to 100 V so long as S1 is kept at 1 V. Thus, because the source optics can be raised to +100 V and the collision cell can only be dropped to −100 V, we have a 200 V range for the entire tSID experiment.

3. Results & discussion

3.1. Tandem SID of tetramers

Two model tetrameric protein complexes were fragmented by tSID: 53 kDa streptavidin and 103 kDa concanavalin A. We begin with streptavidin in order to compare our tSID product ion distributions to those previously obtained on a Q-IM-TOF [60]. Streptavidin was charge reduced with TEAA to produce predominantly 10+ and 11+ charge state precursors on the FT-ICR (Fig. 2a). Charge reduction with TEAA is used because our group and others have found that charge-reduced protein complexes give fragmentation patterns more consistent with native structures, although broader peaks result [63,64]. In general, source conditions were kept cold in order to maintain native non-covalent interactions. We have previously observed significant changes in fragmentation when using in-source activation [65], suggesting overall conformational changes by CID in the source ion optics, and so any broad peaks observed in this manuscript are the result of purposefully soft instrument conditions (and protein heterogeneity in a few cases).

When subjected to low energy SID-Q at 50 V, the predominantly 10+ and 11+ charge-reduced tetramers fragment almost exclusively to 5+ and 6+ dimers (Fig. 2b), as also observed by Quintyn et al. on a Q-IM-TOF platform [60]. SID is well known to yield symmetric charge partitioning (i.e. fragments retain an amount of charge proportional to their mass) [66] and fragments consistent with subunit arrangement and interfacial areas [39]. For streptavidin, the predominant fragments are dimers because of the dimer-of-dimers arrangement (i.e. unequal interfacial areas between adjacent monomers) [41]. Note that the first stage of SID (SID-Q) takes place prior to the quadrupole and so no mass selection is possible in this case. Even so, these data suggest that SID-Q fragmentation is consistent with prior SID implementations in our laboratory in producing native-like fragments, though the extent of unfolding cannot be measured on this system [41,67–70]. The observation of strictly dimers – without any highly charged monomers - from low-energy SID indicates that the tetramer precursors remain native throughout the source ion optics under the conditions illustrated in Fig. 1, despite the use of high rf potentials for radial confinement in the ion funnels. These data demonstrate SID in the entrance lens of a quadrupole, an arrangement that causes signal loss but allows estimation of the dissociation time of the complexes that have undergone surface collisions, described later.

Because SID-Q takes place in the entrance lens of the quadrupole, we hypothesized that some precursors may not have enough time to fragment in the short time it takes to traverse the ~11 mm rf-only prefilter (estimated as ~25 μs based on retention of 15% of the collision energy as kinetic energy) [71,72] prior to mass selection in the analyzer section of the quadrupole, and therefore the fragments themselves might not be isolatable if fragmentation takes place in the analyzer, post-filter, or collision cell. Although the fragmentation kinetics of small peptides are well studied [30,73,74], less is known about the SID fragmentation kinetics of macromolecules, protein complexes in particular. One exception is a recent study from the Prell group which described energy deposition by collision-induced unfolding and surface-induced unfolding [75].

After SID-Q 50 V of streptavidin tetramer we were able to isolate both the 5+ and 6+ dimer in the quadrupole (Fig. 2c and d),

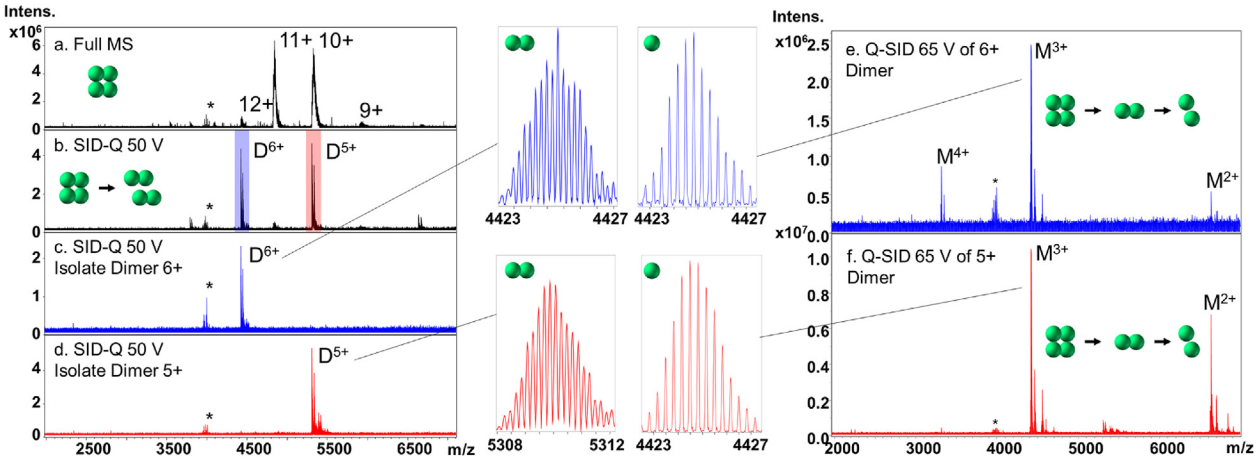

Fig. 2. Tandem SID of streptavidin tetramer: (a) Full scan mass spectrum of streptavidin charge reduced with TEAA, (b) SID-Q 50 V of the entire charge state distribution, producing primarily dimers, (c) and (d) isolation of the 6+ and 5+ dimers, respectively, in the quadrupole after SID-Q, (e) and (f) Q-SID 65 V of the 6+ and 5+ dimers after SID-Q 50 V. Panels in the middle show the observed isotopic distributions corresponding to 5+ and 6+ dimer and 3+ monomer. A variable number of methionines is observed on the oligomers, resulting in apparent peak splitting. * = noise.

implying that at least *some* of the precursor population fragmented either within the 11 mm pre-filter or in the 176 mm analyzer section. Fragmentation of a protein complex, breaking only non-covalent bonds, is reasonable in a 25 μs timeframe based on unfolding studies for small proteins where multiple tertiary interactions must be broken [76].

Fig. S1 shows the (a) full scan as well as (b) Q-SID and (c) SID-Q spectra of the 9+ through 11+ streptavidin tetramers at higher energy, with 85 V of acceleration, where monomer, dimer, and trimer subcomplexes are produced rather than just dimers. Clearly the two modes of SID, (b) in the collision cell entrance lens and (c) in the quadrupole entrance lens, produce similar spectra and any differences in relative abundance can be accounted for by considering the differences in field shape, acceptance, and transmission between the quadrupole analyzer and the hexapole collision cell. The quadrupole clearly biases slightly against the higher *m/z* product ions in panel (c), but the differences between (b) and (c) are quite minor and can be minimized with optimization of the quadrupole rf amplitude.

Similar to the 50 V SID-Q experiment just discussed, at 85 V collision voltage every SID-Q fragment could be isolated (Figs. S1e–i), including the monomers. Moreover, when the Q1 mass was set at *m/z* 5000 (i.e. low mass cutoff of ~*m/z* 3900 in the quadrupole) and the SID-Q experiment was repeated, no monomer 4+ or 5+ was observed (spectrum d). When dimer 5+ was isolated (panel h), no monomer was observed. This implies that the monomers are not produced in the collision cell after SID-Q, i.e., by slow secondary dissociation of the dimer or by CID after SID. These data indicate that 1) the monomers are generated from fast dissociation directly from the tetramer (e.g. Q-> D+2M or Q->4M) and/or 2) from two fast consecutive dissociation steps [Q->2D-> D+2M (or 4M)], both of which occur within 10^1–10^2 μs in the quadrupole.

Because SID fragments could be isolated in the quadrupole, it was possible to conduct a second stage of SID to accomplish the full tSID experiment. For example, SID of the 6+ dimer (produced from SID-Q 50 V) in Fig. 2e creates 2+ through 4+ monomer, with the dominant and average charge being 3+. Approximately 70% of the signal intensity can be attributed to the 3+ monomer, 20% to the 4+ monomer, and 10% to the 2+ monomer (likely not equal to the 4+ monomer due to transmission differences). The ultrahigh resolution of the FT-ICR makes the assignment of the peak at *m/z* 4424 unambiguous because the isotopic spacing is consistent with a 3+ monomer rather than an unfragmented 6+ dimer (compare zoom in panels in Fig. 2). Similarly, fragmentation of the 5+ dimer (Fig. 2f) produces 2+ and 3+ monomers. Although these fragments do not overlap with the precursors, the isotopic resolution is still useful for assigning charge states, particularly when the number of charge states of a given species may be too low for accurate reconstruction of the absolute mass domain using deconvolution algorithms. We will show examples later where only a single charge state was observed for some fragments. The resolution obtained in this experiment using a 2.3 s transient at *m/z* 4424 was m/Δm = 60,000 and at *m/z* 5309 was m/Δm = 48,000.

The charge distributions of the fragment ions from this tSID experiment are consistent with those found by Quintyn et al. via a tSID experiment on the Q-IM-TOF platform [60]. The horizontal slices from the SID-IM-SID mobiligram showed 3+ and 2+ monomers as the primary fragments for the 5+ dimer and 2+ through 4+ monomers as primary fragments for the 6+ dimer. tSID of the trimer 8+ species (produced at a higher SID-Q voltage of 85 V) yielded 3+ through 6+ dimer as well as an abundance of monomer 2+ through 5+ (Fig. 3), with dimer making up approximately 21% of the integrated intensity and monomer making up the remainder. Based on a symmetric charge partitioning model we expect two-

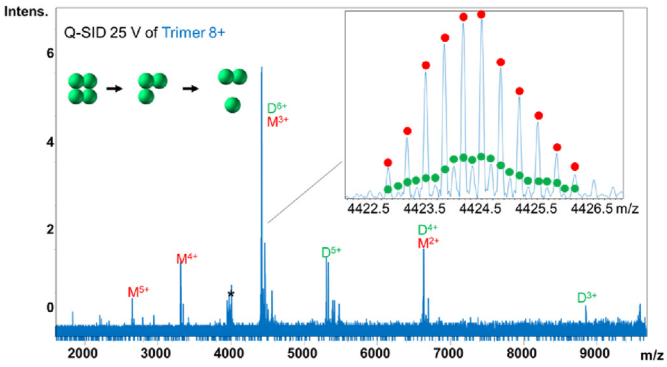

Fig. 3. Q-SID 25 V of the 8+ trimer produced from SID-Q of streptavidin tetramer at 85 V * = noise.

thirds of the total charge to remain with the dimer, or 5.3 charges, on average, in agreement with the observed partitioning. The masses and charges of the individual fragments are also complementary, i.e. dimer 3+ and monomer 5+ are observed as the lowest and highest charge states of the dimer and monomer.

We were also able to carry out SID-Q-CID experiments because the SID-Q surface is farther away from the solariX collision cell compared to the Q-SID surface in the collision cell's entrance lens. Fig. S2a shows CID 70 V of the 6+ dimer produced by SID-Q 50 V of the tetramer. In this case only 3+ monomer was observed and is differentiated from unfragmented 6+ dimer by isotopic spacings. The observation of exclusively monomer with half the charge of the precursor is not typical for CID of protein complexes and their subunits but may indicate that both monomers remained folded after the first (SID) stage of activation; symmetric charge partitioning can occur in CID when the precursor is of sufficiently low charge. Presumably Quintyn et al. also found that SID-IM-CID of 6+ dimer gave 3+ monomer, though without the high resolution of the FT-ICR and without a second stage of mobility after CID it was unclear from the horizontal slices of the mobiligram whether the ion intensity was leftover dimer 6+ or monomer 3+. This experiment highlights a key advantage of the FT-ICR implementation. In contrast, CID of the 5+ dimer generates 2+ through 4+ monomer (Fig. S2b), with slightly more charge asymmetry than the SID spectrum but an overall similar charge state distribution. The 1+ monomer (*m/z* 13,272), the complement of the 4+ monomer, is likely not observed due to lower transmission under these conditions, which were optimized for *m/z* 1000 to *m/z* 8000. Note that the peaks indicated with a caret are adducts formed from gas-phase adduction of a diisononyl phthalate (monoisotopic mass of the neutral: 418.308 Da, measured *m/z* 419.316 as protonated ion) with the protein complexes. We are currently working to isolate the source of the reaction but it is nonetheless interesting that these adducts are formed so readily in the collision cell.

A second tetrameric protein complex we probed by tSID was concanavalin A (conA, 103 kDa). Charge reduction with TEAA yielded 12+ through 15+ tetramers along with some dimers and monomers in solution, which is typical for conA (Fig. S3a). Fragmentation of this whole mixture of structures and charge states produced primarily monomers via SID-Q 80 V, but note that the monomers can originate from the solution dimers or tetramers. A high collision energy was chosen for the first stage of this experiment in order to generate sufficient product ion yield for the second stage, even though the high energy results in observation of a significant amount of monomer. Even so, the monomers were not probed further. Instead, the dimer 7+ was mass selected and fragmented again by (c) Q-SID 90 V and (d) CID 70 V, with SID

producing predominantly 3+ and 4+ monomers and CID yielding poor S/N under similar conditions. Q-SID 90 V of the 10+ trimer generated 6+, 7+, and 8+ dimers as minor species and 3+ through 6+ monomers as the most abundant fragments (spectrum e).

One interesting observation from this experiment is that peak broadening and a loss of absolute mass were observed in the second stage of SID (e.g. spectra c and e) compared to the first stage (spectrum b). This is due to loss of water and/or buffer ions after surface collision. The panels on the right-hand side of Fig. S3 give a closer look at the isotope distributions, with water loss marked. The theoretical average *m/z* of the 4+ monomer is *m/z* 6394.1507, and the lowest measured *m/z* in panel (b) is *m/z* 6415.691. Therefore the loss of mass may be extra solvent or ammonia molecules. However, in panel (c) we see isotope distributions with masses less than the theoretical mass of the monomer, and so it's possible that covalent cleavages leading to loss of water are occurring.

Covalent loss of water can also be observed when comparing SID of streptavidin tetramer 15+ at (Fig. S4a) 30 V and (Fig. S4b) 80 V. The theoretical average *m/z* of the 4+ monomer is *m/z* 3318.8864, in agreement with panel (a). However, at higher collision energy, a loss of water (18.010 Da loss measured) is observed, generating peaks below the theoretical mass. Therefore, the loss of water in this particular case can be attributed to covalent cleavages in the monomers. For concanavalin A, we believe the broadening of the monomer peaks after the second stage of SID can be attributed to both loss of extraneous water/buffer from the subunits as well as covalent cleavages within the monomers.

3.2. Tandem SID of pentamers

Two cyclic homopentameric protein complexes, 58 kDa cholera toxin B (CTB) and 115 kDa C-reactive protein (CRP), were chosen for this study. When charge reduced with EDDA, nESI of CTB produces 12+ through 14+ pentamers (Fig. 4a). When fragmented by SID-Q, monomer through tetramer are observed because CTB is a cyclic complex (Fig. 4b). We were able to conduct tSID experiments of the mass-selected dimer 5+ (Fig. 4c), trimer 7+ (Fig. 4d), and tetramer 9+ (Fig. 4e) by selecting each species with the quadrupole after the first state of SID. The dimer 5+ fragments primarily to monomer 2+ and 3+ of equal abundance, the trimer 7+ fragments to monomer 2+ and 3+ as well as dimer 3+, 4+, and 5+ (e.g., [one monomer 3+ and two monomer 2+], or [one dimer 4+ and one monomer 3+] or [one dimer 5+ and one monomer 2+]), and the tetramer 9+ fragments to monomer 2+, 3+, and 4+, dimer 3+, 4+, and 5+, and trimer 5+ and 6+ (e.g., [one trimer 6+ and monomer 3+] or [dimer 4+ and dimer 5+]). The insets show an overlap peak at *m/z* 5804, with dimer 4+ and monomer 2+ baseline resolved with a 2.3 s transient. Panel e was obtained with a longer 4.6 s transient but trimer 6+ and dimer 4+ remain unresolved from each other. This example again highlights the utility of isotopic resolution when conducting tandem SID experiments, as the trimer 6+, dimer 4+, and monomer 2+ would not be distinguishable on lower-resolution platforms without ion mobility after tSID. The resolution obtained in this experiment at *m/z* 5804 was (c,d; 2.3 s transient) m/Δm = 45,000 and (e, 4.6 s transient) m/Δm = 88,000.

C-reactive protein, when charge reduced with TEAA, gives 16+ through 19+ charge states on the FT-ICR (Fig. S5a), and produces monomer through trimer by SID-Q at 55 V. Due to the low intensities of the trimer species when subject to SID-Q 55 V (Fig. S5b), only dimers could be isolated for tSID experiments. More trimer and tetramer were observed at lower collision energy but the absolute scattered ion yield was too low for tandem experiments. Nonetheless, the dimer 7+ species was selected and subjected to Q-SID 55V, producing monomer 3+ and 4+ (Fig. S5c). This result is identical to that obtained by Quintyn et al. on a Q-IM-TOF platform [60], with an average of 3.5 charges being retained by each monomer, i.e. symmetric charge partitioning.

3.3. Tandem SID of a homohexamer

HFQ65, a 43 kDa truncated RNA chaperone, was chosen as a model cyclic homohexamer for tandem SID experiments. Fig. 5a shows the HFQ65 precursors after charge reduction with TEAA. On average, the precursors have between 9 and 10 charges. The SID-Q spectrum at 35 V (Fig. S6, top) and 55 V (Fig. 5b) closely resemble spectra previously acquired by Q-SID with two different

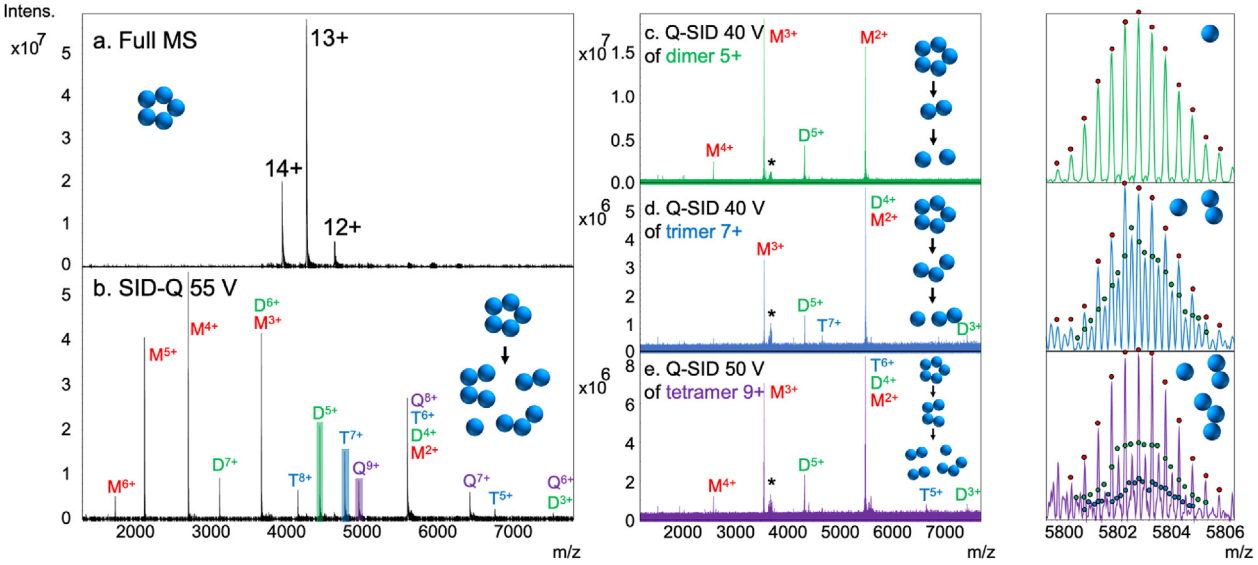

Fig. 4. Tandem SID of a cyclic pentamer: (a) Full scan mass spectrum of cholera toxin B charge reduced with EDDA, (b) SID-Q 55 V of the entire charge state distribution, producing fragments over a range of oligomeric states due to the cyclic arrangement of the subunits, (c) Q-SID 40 V of the isolated dimer 5+ after SID-Q 55 V, (d) Q-SID 40 V of the isolated trimer 7+ after SID-Q 55 V, and (e) Q-SID 50 V of the isolated tetramer 9+ after SID-Q 55 V. The inset isotopic abundances in (c), (d), and (e) indicate overlapping dimer and monomer at *m/z* 5803 for SID of the trimer and tetramer but not the dimer. * = noise.

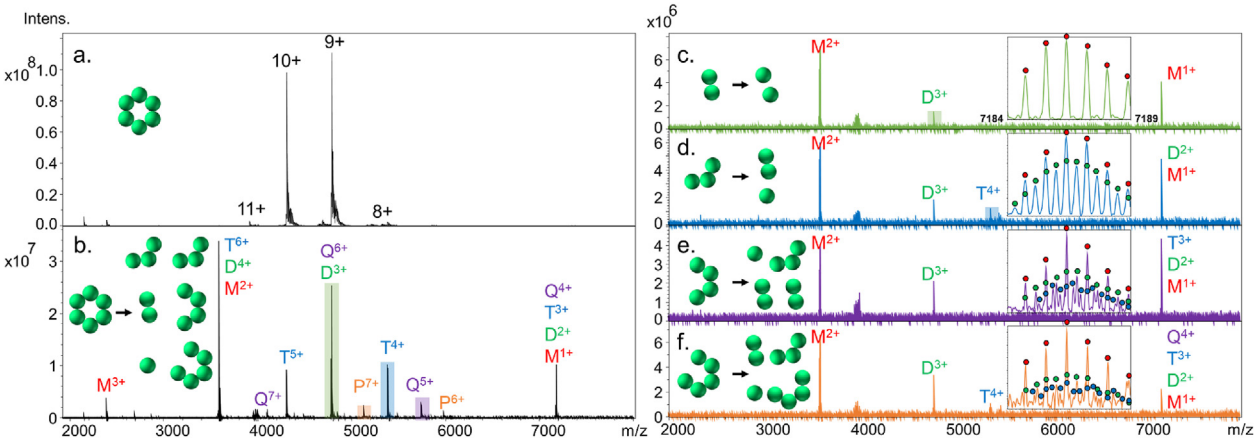

Fig. 5. Tandem SID of a cyclic hexamer: (a) Full scan mass spectrum of HFQ65 charge reduced with TEAA, (b) SID-Q 55 V of the entire charge state distribution, producing fragments over a range of oligomeric states due to the cyclic arrangement of the subunits, (c) Q-SID 50 V of the overlapping dimer 3+ (dominant) and tetramer 6+ (minor) at *m/z* 4791, (d) Q-SID 30 V of the trimer 4+ at *m/z* 5390, (e) Q-SID 50 V of the tetramer 5+ at *m/z* 5749, and (f) Q-SID 50 V of the pentamer 7+ at *m/z* 5133. Isotopic abundances are shown in the insets for the peak at *m/z* 7186 in (c)–(f) for (c, d) a 2.3 s transient or (e, f) a 4.6 s transient. * = noise.

generations of SID devices on the FT-ICR platform [35,62]. Monomer through pentamer are all produced from fragmentation of the cyclic hexamer because all the interfacial interactions between adjacent monomers are equal. At both energies we were able to isolate several species with the quadrupole after SID-Q (Fig. S6 shows isolation of several species after SID-Q 35 V, for example). The ability to isolate the large and small oligomers once again implies fragmentation of the hexameric species within tens to hundreds of microseconds. In contrast to the streptavidin example, when the larger oligomers were selected by the quadrupole, some secondary dissociation was observed. For example, when the 5+ trimer was selected, dimer 3+ and monomer 2+ were detected, although it is unclear if these dissociation products were from CID in the collision cell or secondary dissociation from SID-Q. Even so, it is clear that most of the isolated species remain intact after mass selection, allowing tSID experiments to be performed.

For tSID we chose SID-Q 55 V for the first stage of activation in order to yield more precursor signal for the second stage of SID. Panels (c-f) in Fig. 5 show tSID spectra of (c) the 3+ dimer (150 eV), (d) the 4+ trimer (120 eV), (e) the 5+ tetramer (250 eV), and (f) the 7+ pentamer (350 eV). In each case the charge partitioning scales well with the mass of the oligomer, implying that even after a second surface collision the monomers of the ring-like complex remain in a folded (vs. unfolded) state, though based on this data we cannot conclude that the sub-rings have not collapsed to maximize intermolecular stabilization. The high resolution of the FT-ICR was useful for determining the species at *m/z* 3593 (only monomer), *m/z* 4791 (only dimer), and especially *m/z* 7186 which involved several oligomers. Using a 2.3 s transient, we can conclude that the peak at *m/z* 7186 consists of (c) only monomer 1+ from dimer 3+ (note the 6 carbon isotopes in the span of 6 *m/z* from *m/z* 7184 to *m/z* 7189), (d) a small amount of monomer 1+ and a substantial amount of dimer 2+ from trimer 4+, and using a 4.6 s transient (e) monomer 1+, dimer 2+ and trimer 3+ from tetramer 5+. As the pentamer was low in relative abundance after SID-Q, its tSID fragment ions were also of low abundance. Panel (f) was obtained using the maximum accumulation time of the instrument (100 s) but still yielded insufficient S/N to conclusively identify tetramers. Even so, it is clear that several species are present in this panel, and based on the fragmentation of the dimer through hexamer it is likely that tetramer 4+ is present in the fragments of the pentamer 7+. The resolution obtained at *m/z* 7186 in this experiment was (2.3 s transient) m/Δm = 35,000 and (4.6 s transient) m/Δm = 85,000. While longer transients can increase the resolution further, the already-low signal in these tSID experiments coupled with a longer transient yielded spectra with insufficient S/N. Generally ~9 s transients were the longest useful transients with sufficient S/N, but shorter transients were used in this work to obtain higher S/N.

3.4. Tandem SID of a heterohexamer

We next chose to illustrate tSID with the heterohexamer toyocamycin nitrile hydratase. SID has previously been utilized to provide key information regarding the relative interfacial strengths and connectivity between the two alpha (21.2 kDa each), two beta (10 kDa), and two gamma subunits (13.6 kDa with His tag, 11.4 kDa without tag) [37,43]. The TNH protein used in this work contains a 2.2 kDa His tag on the gamma subunits; both tagged and untagged TNH have been investigated by SID, although fragmentation is charge-state dependent and differs for the tagged and untagged complexes [77]. Song et al. found that the 14+, 17+, and 19+ charge states of the tagged and untagged TNH hexamers had similar fragmentation patterns (for the same charge state), though untagged TNH appeared to more preferentially form αβ dimers as well as the complementary ɣ monomers [77]. Even so, in both cases αβɣ trimers were the prominent SID fragments across a wide energy range due to the *dimer-of-heterotrimers topology*. As of yet, there is no published high-resolution cryo-EM structure for the complex. In contrast, native and denaturing mass spectrometry have instead proven fruitful for investigating TNH [37,43]. In this work we sought to utilize tSID with an intermediate stage of mass selection to decipher differences in structure – observed through variations in SID fragmentation patterns – of the TNH hexamer caused by the addition of the His tag, which is a common treatment in overexpression of proteins. In this section we refer to His-tagged TNH and its His-tagged ɣ subunit as TNH_{His} and $ɣ_{His}$, respectively, with untagged variants referred to simply as TNH and ɣ.

A full scan mass spectrum of TNH_{His} charge reduced with TEAA is provided in Fig. 6a, along with an illustration of the previously-determined interconnectivity [43] of the six subunits for TNH. The charge states observed on the FT-ICR were 13+ through 15+ hexamer, along with some αβ dimers. A single stage SID-Q mass spectrum using 80 V collision voltage is shown in panel b. The prominent fragments are $αβɣ_{His}$ trimers, as has been previously reported [37,43], because the arrangement of the subunits is a

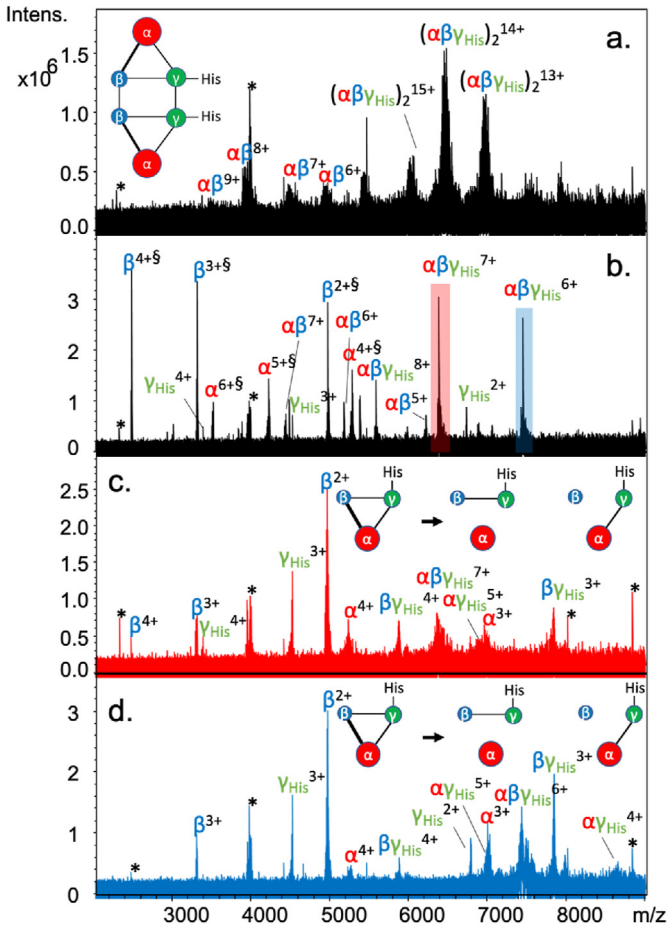

Fig. 6. Tandem SID of a heterohexamer: (a) full scan mass spectrum of His-tagged toyocamycin nitrile hydratase (TNH_{His}) charge reduced with TEAA (note the unassembled αβ dimers), (b) SID-Q 80 V of the entire charge state distribution (§some α and β intensity results from fragmentation of αβ), and Q-SID 80 V of the isolated (c) 7+ and (d) 6+ heterotrimer. * = noise. Please note the presence of a 2.2 kDa His tag on each of the gamma monomers.

dimer of αβγ heterotrimers. Other species observed are αβ dimers (because the interfacial area between these two subunits is largest) as well as monomers. Note that some of the intensity of the α and β monomers originates from the excess αβ dimers in solution because there is no means of isolating species prior to the SID-Q surface collision. A Q-SID spectrum of the quadrupole-isolated heterohexamers confirms this suspicion (Fig. S7b), with heterotrimers as the dominant fragments and much lower abundances of α and β but similar abundance of γ_{His} compared to Fig. 6b. We are interested in whether the $\alpha\beta\gamma_{His}$ trimers with a large His-tag on γ_{His} fragment differently from the untagged trimers that we previously fragmented by tSID.

We were able to isolate the $\alpha\beta\gamma_{His}$ heterotrimers to conduct tSID of the 7+ heterotrimer (Fig. 6c, Q-SID 80 V) and 6+ heterotrimer (Fig. 6d, Q-SID 80 V). The dominant fragments in these spectra are α, β, and γ_{His} monomers with two complementary dimers, $\beta\gamma_{His}$ and $\alpha\gamma_{His}$. The fragmentation patterns of the 6+ and 7+ trimer are markedly similar, with slightly lower charge states being observed for the fragments of the 6+ trimer (blue trace). The lack of αβ dimer, the complement to γ_{His} monomer, in these tSID spectra is unexpected, in that the interfaces between these subunits are thought to be the strongest for the untagged hexamer, and so one would expect the $\alpha\beta\gamma_{His}$ trimer to fragment to complementary αβ dimer and γ_{His} monomer. Instead, $\beta\gamma_{His}$ dimer appears to be the dominant fragment from tSID of the $\alpha\beta\gamma_{His}$ trimer. The presence of the 2.2 kDa His tag on the gamma monomers changes the tSID fragmentation compared to that observed by Song et al., who only conducted tandem SID experiments on the untagged TNH complex and found major fragments to be αβ dimer and γ monomer, the expected low-energy product ions based on interfacial areas for the untagged hexamer [43,77].

In order to validate our results, we conducted tSID experiments on a Synapt G2 equipped with two SID devices. A 'Gen 3' split lens device was placed prior to the trap collision cell (and after the quadrupole) as a replacement for the dynamic range enhancement lens [35], and a 'Gen 1' SID device was placed just after the trap but prior to the ion mobility cell [67,78]. This instrument configuration allows quadrupole-isolated precursors to be fragmented by SID just prior to the trap. Then the fragment ions from this first SID stage are stored and thermalized in the trap for <20 ms, after which they are transferred into the second SID cell for further fragmentation. The tSID fragments generated by the second SID cell are then mobility separated and detected by TOF mass analysis. This configuration does not allow for mass selection between SID stages but we can still infer structural information from the tSID patterns and compare the results to the FT-ICR data.

We begin by conducting tSID on the *tagged* heterohexamer (TNH_{His}) on the Synapt G2 (without *m/z* selection for direct comparison with the ICR data). Fig. 7 shows (a, b) a single stage SID spectrum of the 13+ through 15+ charge states of the heterohexamer in the 1D *m/z* domain and the 2D *m/z* and arrival time domains. Fig. 7a is remarkably similar to Fig. 6 and Fig. S7b, indicating that the SID configurations in the Synapt and solariX produce similar results.

Next we conducted a second stage of SID on TNH_{His} via the Synapt G2 platform, though without mass selection of any of the ions appearing from the first SID stage. Panels (c) through (h) show mass spectra and corresponding ion mobility plots for the tandem SID experiment in order of increasing second stage collision energy, from 80 V in the second stage to a maximum of 160 V in the second stage. From these spectra we can infer that tSID of TNH_{His} produces abundant β and γ_{His} monomers, as was the case on the solariX. Now focusing on the heterodimers generated in the tSID experiment, we find that the heterodimer αβ remains a similar relative abundance in Figs. S7c,e,g as the second stage SID energy is increased. In contrast, the dimers $\beta\gamma_{His}$ (particularly 4+) and $\alpha\gamma_{His}$ (particularly 5+) clearly increase in intensity as the second stage SID energy is increased. These results are similar to those obtained on the FT-ICR. Because isolation was possible between SID stages on the FT-ICR we can conclude that SID of the $\alpha\beta\gamma_{His}$ produces monomers and $\beta\gamma_{His}$ dimers as the most abundant fragments, but $\alpha\gamma_{His}$ dimers are also present in low abundance. Virtually no αβ, the *expected* tSID fragment of TNH trimers, is observed for TNH_{His} trimers.

We next conducted single stage SID experiments on untagged TNH in order to deduce structural difference from comparisons of SID patterns. As shown in Figs. S8a,b, a single stage SID experiment of TNH on the Synapt G2 produces abundant heterotrimer as well as αβ dimers and α and γ monomers. βαγγ tetramers, complementary products to αβ dimers, were also detected in high abundance. This is the expected result given that the interfacial strength of the αβ pair is the strongest within the complex. Notably, the abundance of αβ is much higher compared to tagged TNH, and very little β is generated in the single stage SID experiment. The decrease in β and increase in γ in Fig. S8a compared to Fig. 7a implies a structural difference caused by the His tag on each γ subunit.

After the single stage SID, we conducted tSID experiments on untagged TNH using the Synapt platform (Figs. S8c-h). We are interested in differences in these spectra compared to those from TNH_{His} (Fig. 7). Regarding monomer abundances, we see that the γ

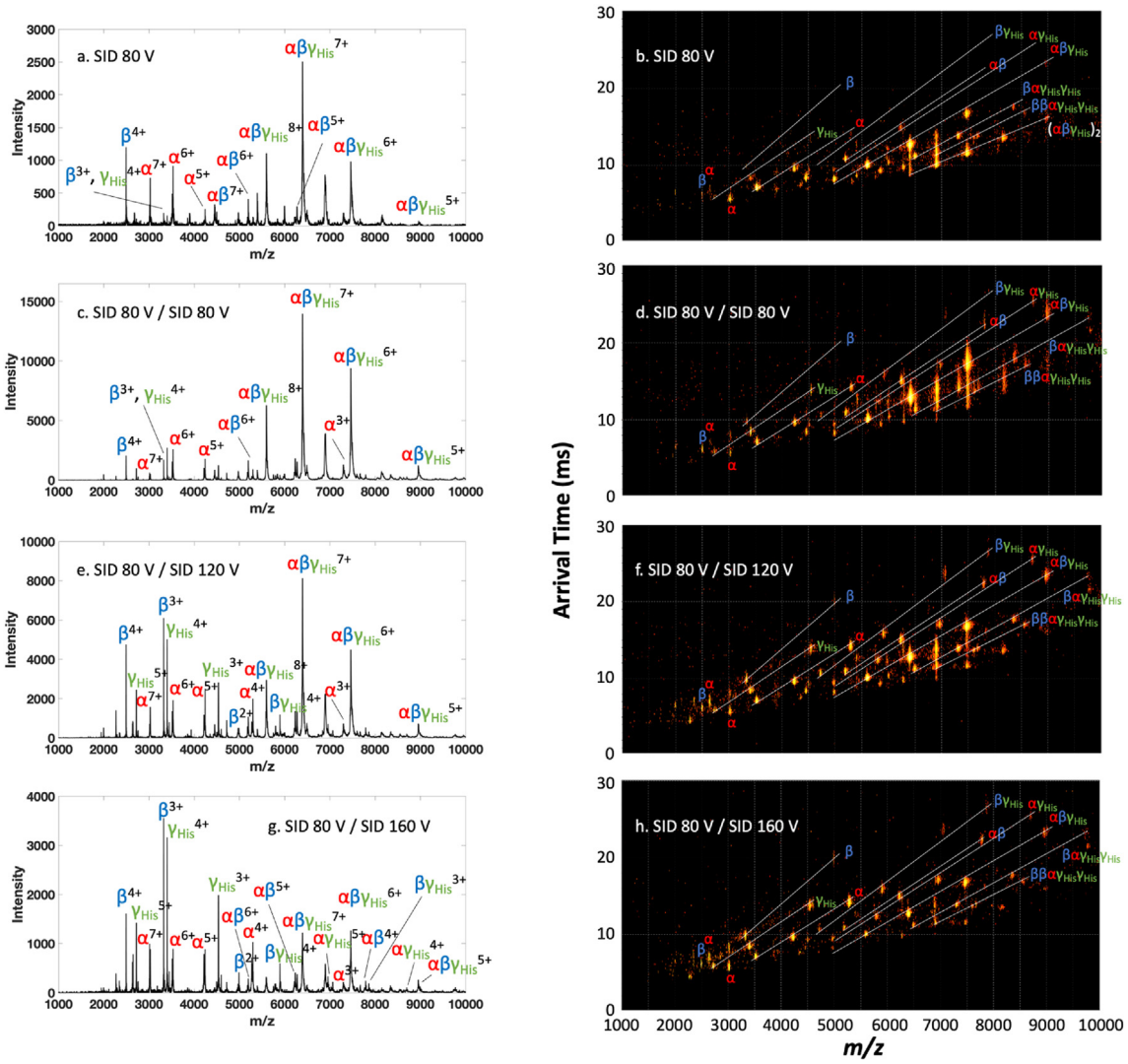

Fig. 7. Tandem SID of His-tagged heterohexamer toyocamycin nitrile hydratase (TNH_{His}) charge reduced with TEAA (13+ through 15+ precursors) on a Synapt G2 modified with SID devices placed just before and just after the Trap cell. (a) A single stage of SID of the 13+, 14+, and 15+ precursors, (c) SID 80 V (pre-trap) followed by SID 80 V (post-trap), (d) SID 80 V followed by SID 120 V, (g) SID 80 V followed by SID 160 V, (b, d, f, and h) the corresponding mobiligrams. Please note the 2.2 kDa His tag is on the gamma subunits.

subunit is easily ejected from both TNH and TNH_{His} and its first-stage SID fragments, but the β subunit is only generated in high amounts from tSID of TNH_{His}, not TNH. Moreover, while tSID of TNH_{His} results in a clear increase in relative abundance of βɣ, the major tSID dimer fragments of TNH are the expected αβ dimer and its complementary ɣ monomer fragment (assuming fragmentation of αβɣ).

Thus, because different dimer and monomer fragments are produced from SID and tSID of TNH and TNH_{His}, we can conclude that the presence of the large 2.2 kDa His tag on the ɣ subunits changes the interfaces within the TNH complex such that the generation of the complementary αβ dimer and ɣ monomer from fragmentation of the heterotrimer is much less preferable, and instead a strong interaction between β and ɣ subunits is observed. These experiments illustrate the utility of tSID for probing heteromers and also demonstrate tSID configurations on both an FT-ICR and a Q-IM-TOF platform (a new configuration compared with our previous tSID publication [60]).

We should note that the differences in collision energies between the FT-ICR and the Synapt G2 (e.g., 1120 eV in FT-ICR vs 2240 in G2 for comparable relative abundances) is likely explained by the thermalization of the ions in the trap collision cell of the G2. In the FT-ICR, there is only a low pressure ($<1.0 \times 10^{-5}$ torr) quadrupole between the two stages of SID, and so the ions remain kinetically and vibrationally excited between stages and require less collision energy in the second stage of activation (and therefore our definition of second stage SID collision energy is strictly inaccurate when the residual kinetic energy from the first collision is ignored), though the excess kinetic energy is only on the order of a few volts multiplied by the ion charge state as measured next via stopping curves. This suggests that the lack of dampening of vibrational excitation between surface collisions is also playing a role in the extent of fragmentation in the FT-ICR tSID.

3.5. Kinetic energy retention after surface collision

A knowledge of the axial ion kinetic energy after the SID-Q collision would be useful for modelling purposes in order to design better SID ion optics as well as for determining the lifetimes of the precursor ions in the pre-filter and quadrupole mass filter.

Using streptavidin 10+ and 11+ (i.e. charge reduced with TEAA), we conducted a series of crude stopping curve experiments after

SID-Q of the tetramers by varying the bias voltage on the quadrupole post-filter and recording the ion intensity of each fragment as a function of voltage. This experiment was conducted in transmission mode and at two SID collision voltages, 45 V and 85 V. Fig. S9a shows the stopping curve for transmission of the streptavidin tetramers, indicating an effective birth potential of 4.5 V (post-filter voltage at which half maximum intensity was observed). The sharpness of the signal dropoff at 4.5 V indicates a thermalized distribution of ions with well-defined kinetic energies, a near-ideal starting distribution for this experiment.

Total ion counts for the SID experiments are shown in panels (b) and (c), top panels, as well as extracted ion intensities for either remaining tetramer (11+ and 9+) or SID fragment ions (dimers and monomers). Note that the SID collision voltage is defined as the difference in potential between the skimmer 2 and the SID-Q surface, which was held at 1 V for the entirety of this experiment. Because the surface, quadrupole pre-filter, and quadrupole analyzer were all maintained at 1 V, there was no acceleration between surface and post-filter.

If we determine the post-filter voltage at which only 50% of the original ion intensity remains, as shown in each stopping curve, we can deduce the approximate average axial ion kinetic energy retained after the surface collision. At SID 45 V, for example, the percentage of kinetic energy retained along the axial direction, on average, was approximately (9.2 V−1.0 V)/45 V = 18% of the collision energy. At a collision voltage of 85 V, the average percentage of kinetic energy retained was approximately 9.4% of the collision energy. These values are in reasonable agreement with kinetic energy retention reported by Hanley and coworkers [79], who determined scattered parent ion kinetic energy retentions of 24%, 21%, and 17% for linear peptides, cyclic dipeptides, and four-peptide rings. Although a steel surface is used in our tSID work, compared to a hexanethiolate monolayer on Au(111) in Hanley's work, the steel is expected to be coated with organics present in the vacuum chamber and a hexanethiolate layer is not long enough to be considered well-packed and rigid at room temperature. The Futrell group reported kinetic energies of 1−2 eV after benzene molecular ions had collided into a SAM surface at a 45° angle, i.e. 10%−20% kinetic energy retention as a percentage of the collision energy [72], and others have reported similar kinetic energy retentions around 10%−25% of the collision energy [80,81]. If all ions were "born" at the surface in a shattering mechanism, we might also expect sharper stopping curves for the SID products rather than the measured broad tails that suggest a range of product ion orientations and internal and kinetic energies. Nonetheless, the observation of 1) different stopping potentials and 2) different high-energy tails for each species is consistent with *fragmentation of the precursors prior to the post-filter*. It is not the purpose of this paper to discuss mechanistic findings in detail; we use these stopping curves only to determine the average axial ion velocity (and distribution) and so to determine the average residence time of the ions in the quadrupole sections.

3.6. Lifetimes of protein complexes after surface collision

Now that we have approximations for the ion kinetic energy at two selected collision energies within the quadrupole sections, we can calculate the amount of time the ions spend in the quadrupole pre-filter before being transmitted through the quadrupole mass analyzer, as well as the amount of time the ions spend within the analyzer rods prior to the post-filter.

Assuming a collision voltage of 45 V (405−495 eV for the 9+ to 11+ tetramers) and kinetic energy retention as a percentage of the collision energy along the quadrupole axis as (10 V−1 V)/45 V = 20% (Fig. S9b, D^{5+}, where 10 V corresponds to the post-filter voltage at which the D^{5+} intensity is reduced to 50% and 1 V is the surface voltage), a dimer 5+ ion of streptavidin (*m/z* 5322) will have a kinetic energy along the quadrupole axis of 45 eV and a velocity of 570 m/s. Therefore, the ion will reach the end of the pre-filter region (13 mm total distance traveled: 2 mm between surface and pre-filter, 11 mm pre-filter length) within 23 μs and will reach the end of the quadrupole analyzer (190 mm total including 176 mm long quadrupole analyzer) within approximately 330 μs. At SID 85 V (765−935 eV for 9+ to 11+ tetramers), the dimer 5+ velocity is approximately 500 m/s and the time-of-flight to the quadrupole analyzer and post-filter is 26 μs and 380 μs, respectively, because a lower percentage of the collision energy is left as residual kinetic energy compared to SID 45 V. Although a 'shattering' mechanism was previously proposed by Laskin and Futrell [82−85], work on cyclic and octapeptides by Hase [79,85] and recent work by Barnes [86] has shown that the extent to which peptides undergo very fast fragmentation decreases significantly even as peptides reach lengths of 8 amino acids. In the case of our experiments, it may be that the streptavidin tetramer spends some time (tens of μs) in the prefilter and/or analyzer rods as a transiently stable species before fragmenting to trimer, dimers, and monomers, as it takes some number of rf cycles to cause collision of the ions with the quadrupole rods in rf/dc mode. The timing (<23−380 us) is long enough to allow for protein complex dissociation separated from the collision event. The successful isolation of dimers and monomers of streptavidin (Fig. S1) implies that at least some portion of the precursor population must fragment within this timescale, but the exact proportion is unknown and would be difficult, if not impossible, to quantify with the current instrument due to transmission differences as a function of the quadrupole rf/dc potentials. Even so, we do know that larger complexes require higher collision energies to fragment and that we have larger complexes that don't fragment significantly at the energy range available in our SID devices in multiple instruments. These observations are consistent with typical RRKM models of fragmentation. Future work will explore the fragmentation timing in more detail but it is not the topic of this paper.

3.7. A comparison of two designs: advantages and limitations

This paper reports only the second instrumental configuration for tSID of protein complexes (Table 1, column 2) and the first on an ultrahigh resolution FT-ICR platform. A previous design developed in our laboratory (Table 1, column 3) was implemented on a Synapt Q-IM-TOF platform [60]. On the Synapt, two custom SID devices, each consisting of 10 independently controlled electrodes were placed prior to and after the ion mobility cell by truncating the 'Trap' and 'Transfer' collision cells by approximately 3 cm each. The design reported herein utilized two three-lens devices (each ~3 mm in length) replacing the entrance lenses of the quadrupole mass filter and the hexapole collision cell, with five independent voltages (two voltages used for device 1 and three for device 2).

Precursor and product ions were correlated on the Q-IM-TOF through an intermediate stage of ion mobility separation; horizontal slices from the arrival time vs. *m/z* mobiligrams could be used to relate precursor and product ions. Note that there was no isolation of a single ion mobility drift time in this case, only a separation in time that serves as a selection, allowing each species eluting from the IM cell to be collided into the surface. In the current work, an intermediate stage of mass selection/isolation with a quadrupole was used to correlate subcomplexes and their fragments. The IM separation on the Synapt is able to retain higher ion throughput because no isolation step precedes the second SID stage but could suffer from oligomers with overlapping horizontal slices (product ion spectra) if two species with different *m/z* have similar

Table 1
Instrumentation for tandem SID of protein complexes.

	SID-Q-SID (this work)	SID-IM-SID [60]
Instrument	15 T SolariX XR FT-ICR	Synapt G2-S Q-IM-TOF
SID Device 1	 SID-Q	 Trap-SID
SID Device 2	 Q-SID	 Transfer-SID
Total # of SID Electrodes	6 (3 for SID-Q, 3 for Q-SID)	20
# of independent SID voltages	5 (2 for SID-Q, 3 for Q-SID)	20
Truncated elements	Quadrupole and collision cell entrance lenses replaced	Trap and Transfer SRIGs
Total SID length	5.75 mm	68 mm
Selection mechanism after first SID	343 kHz quadrupole	IM used for separation of precursors but not selection

drift times. Similarly, the horizontal slices in the mobiligrams are unable to differentiate tSID ions with the same *m/z* (which would require a second stage of ion mobility), or precursor and product ions from the second SID that have the same *m/z* (e.g. dimer 6+ and monomer 3+). The quadrupole used in this work minimizes contamination from other *m/z* values but cannot separate different conformations (with same *m/z*) nor can it separate different oligomers that overlap in *m/z*. SID spectra are particularly prone to the latter issue due to symmetric charge partitioning, as observed here with HFQ65 hexamer. A useful feature of the ultrahigh resolution platform when fragmentation of subcomplexes produces narrow charge state distributions (one charge state in some cases) is the ability to resolve tSID fragments without ion mobility, an advantage over the Q-IM-TOF implementation. The ion throughput in the FTICR quadrupole configuration, however, is quite low, owing to the low efficiency of transmission of SID products into the fringing field of the quadrupole pre-filter and analyzer, especially in rf/dc mode. We chose to place the first stage of SID in the quadrupole chamber as 1) it is much more accessible than the source region (the entirety of which must be removed from the front of the instrument in order to modify), 2) it is maintained at low pressure ($<1 \times 10^{-5}$ mbar), and 3) we wished to provide preliminary insights into the kinetics of fragmentation after SID as well as calculate the kinetic energy retention after SID in order to better understand SID fundamentals. This would not have been possible if the SID-Q had been placed further into the source region. Even so, we recognize that the SID placement likely compromised the SID-Q sensitivity.

4. Conclusion

In this work we implemented two stages of surface-induced dissociation with an intermediate mass selection step on an ultrahigh resolution FT-ICR platform. Protein complexes were dissociated into subcomplexes indicative of their native connectivity through a first stage of SID in the entrance lens of a quadrupole mass filter (SID-Q). Subcomplexes were then mass-selected in the quadrupole despite only tens of microseconds of residence time prior to entering the quadrupole analyzer, hinting at the fast dissociation kinetics of these macromolecules. Mass-selected subcomplexes were then dissociated with a second stage of SID in the entrance lens of the collision cell (Q-SID), and the product ions were analyzed in an ultrahigh resolution 15 T FT-ICR cell. In many cases, the isotopic resolution of the FT-ICR was useful for deconvoluting overlapping species which on other lower resolution platforms would remain ambiguous without post-SID ion mobility. Although we were limited to relatively small protein complexes due to power supply constraints, this proof-of-concept study paves the way for other tSID implementations which could be useful on Q-IM-TOF, FT-ICR, and Orbitrap instruments, and the small SID footprint should enable ease of installation in a vendor-neutral manner. Tandem SID capabilities extend the amount of connectivity information obtainable by structural biologists, but optimization of ion collection and transmission after each SID device in order to improve sensitivity is paramount to widespread adoption of tSID technology.

CRediT authorship contribution statement

Dalton T. Snyder: Conceptualization, Methodology, Validation, Formal analysis, Investigation, Writing - original draft, Writing - review & editing, Visualization. **Yu-Fu Lin:** Validation, Formal analysis, Investigation, Writing - review & editing. **Arpad Somogyi:** Writing - review & editing, Supervision, Project administration, Funding acquisition. **Vicki H. Wysocki:** Conceptualization, Writing - review & editing, Supervision, Project administration, Funding acquisition.

Declaration of competing interest

The authors declare that they have no known competing financial interests or personal relationships that could have appeared to influence the work reported in this paper.

Acknowledgements

We thank the OSU Arts and Sciences College Machine Shop for fabricating the SID-Q and Q-SID parts used in this work. We also

acknowledge helpful discussions with Mel Park and Mark Ridgway (Bruker Corporation) and thank Desmond Kaplan (Kapscience) for the design and implementation of the low frequency quadrupole driver. We thank Jorjethe Roca and Sarah Woodson (Johns Hopkins University) for the Hfq samples (NIH R01 GM120425) and the Bandarian group (The University of Utah) for the TNH samples. The FT-ICR was purchased with NIH Award S10 OD018507. This work was supported by the NIH P41 Resource for Native Mass Spectrometry Guided Structural Biology, P41GM128577.

We are pleased to honor Professor Bill Hase with this contribution and would like to acknowledge the many stimulating conversations with Bill that are still driving us to improve our understanding of the kinetics and mechanisms of surface-induced dissociation.

Appendix A. Supplementary data

Supplementary data to this article can be found online at https://doi.org/10.1016/j.ijms.2020.116503.

References

[1] D.F. Hunt, J.R. Yates, J. Shabanowitz, S. Winston, C.R. Hauer, Protein sequencing by tandem mass spectrometry, Proc. Natl. Acad. Sci. Unit. States Am. 83 (17) (1986) 6233–6237, https://doi.org/10.1073/pnas.83.17.6233.
[2] J.E. Syka, J.J. Coon, M.J. Schroeder, J. Shabanowitz, D.F. Hunt, Peptide and protein sequence analysis by electron transfer dissociation mass spectrometry, Proc. Natl. Acad. Sci. U.S.A. 101 (26) (2004) 9528–9533.
[3] G.E. Reid, S.A. McLuckey, 'Top down'Protein characterization via tandem mass spectrometry, J. Mass Spectrom. 37 (7) (2002) 663–675.
[4] J.A. Loo, C.G. Edmonds, R.D. Smith, Primary sequence information from intact proteins by electrospray ionization tandem mass spectrometry, Science 248 (4952) (1990) 201–204.
[5] J.L. Benesch, J.A. Aquilina, B.T. Ruotolo, F. Sobott, C.V. Robinson, Tandem mass spectrometry reveals the quaternary organization of macromolecular assemblies, Chem. Biol. 13 (6) (2006) 597–605.
[6] A.J. Heck, Native mass spectrometry: a bridge between interactomics and structural biology, Nat. Methods 5 (11) (2008) 927.
[7] L. Fornelli, K. Srzentić, T.K. Toby, P.F. Doubleday, R. Huguet, C. Mullen, R.D. Melani, H. dos Santos Seckler, C.J. DeHart, C.R. Weisbrod, K.R. Durbin, J.B. Greer, B.P. Early, R.T. Fellers, V. Zabrouskov, P. Thomas, P.D. Compton, N.L. Kelleher, Thorough performance evaluation of 213 Nm ultraviolet photodissociation for top-down proteomics, Mol. Cell. Proteomics (2019), https://doi.org/10.1074/mcp.TIR119.001638 mcp.TIR119.001638.
[8] M. Rožman, S.J. Gaskell, Charge state dependent top-down characterisation using electron transfer dissociation, Rapid Commun. Mass Spectrom. 26 (3) (2012) 282–286, https://doi.org/10.1002/rcm.5330.
[9] M.B. Cammarata, R. Thyer, J. Rosenberg, A. Ellington, J.S. Brodbelt, Structural characterization of dihydrofolate reductase complexes by top-down ultraviolet photodissociation mass spectrometry, J. Am. Chem. Soc. 137 (28) (2015) 9128–9135, https://doi.org/10.1021/jacs.5b04628.
[10] F.P. Gomes, J.K. Diedrich, A.J. Saviola, E. Memili, A.A. Moura, J.R. Yates, EThcD and 213 Nm UVPD for top-down analysis of bovine seminal plasma proteoforms on electrophoretic and chromatographic time frames, Anal. Chem. (2020), https://doi.org/10.1021/acs.analchem.9b03856.
[11] J.B. Shaw, W. Li, D.D. Holden, Y. Zhang, J. Griep-Raming, R.T. Fellers, B.P. Early, P.M. Thomas, N.L. Kelleher, J.S. Brodbelt, Complete protein characterization using top-down mass spectrometry and ultraviolet photodissociation, J. Am. Chem. Soc. 135 (34) (2013) 12646–12651, https://doi.org/10.1021/ja4029654.
[12] M. Zhou, W. Liu, J.B. Shaw, Charge movement and structural changes in the gas-phase unfolding of multimeric protein complexes captured by native top-down mass spectrometry, Anal. Chem. (2019), https://doi.org/10.1021/acs.analchem.9b03469.
[13] F. Lermyte, F. Sobott, Electron transfer dissociation provides higher-order structural information of native and partially unfolded protein complexes, Proteomics 15 (16) (2015) 2813–2822, https://doi.org/10.1002/pmic.201400516.
[14] K. Breuker, F.W. McLafferty, Native electron capture dissociation for the structural characterization of noncovalent interactions in native cytochrome c, Angew. Chem. Int. Ed. 42 (40) (2003) 4900–4904, https://doi.org/10.1002/anie.200351705.
[15] K. Breuker, H. Oh, D.M. Horn, B.A. Cerda, F.W. McLafferty, Detailed unfolding and folding of gaseous ubiquitin ions characterized by electron capture dissociation, J. Am. Chem. Soc. 124 (22) (2002) 6407–6420.
[16] J.B. Shaw, N. Malhan, Y.V. Vasil'ev, N.I. Lopez, A. Makarov, J.S. Beckman, V.G. Voinov, Sequencing grade tandem mass spectrometry for top–down proteomics using hybrid electron capture dissociation methods in a benchtop Orbitrap mass spectrometer, Anal. Chem. 90 (18) (2018) 10819–10827.
[17] R.A. Zubarev, D.M. Horn, E.K. Fridriksson, N.L. Kelleher, N.A. Kruger, M.A. Lewis, B.K. Carpenter, F.W. McLafferty, Electron capture dissociation for structural characterization of multiply charged protein cations, Anal. Chem. 72 (3) (2000) 563–573, https://doi.org/10.1021/ac990811p.
[18] M.B. Cammarata, J.S. Brodbelt, Structural characterization of holo- and apomyoglobin in the gas phase by ultraviolet photodissociation mass spectrometry, Chem. Sci. 6 (2) (2015) 1324–1333, https://doi.org/10.1039/c4sc03200d.
[19] H. Li, H.H. Nguyen, R.R. Ogorzalek Loo, I.D.G. Campuzano, J.A. Loo, An integrated native mass spectrometry and top-down proteomics method that connects sequence to structure and function of macromolecular complexes, Nat. Chem. 10 (2) (2018) 139–148, https://doi.org/10.1038/nchem.2908.
[20] D.P. Little, J.P. Speir, M.W. Senko, P.B. O'Connor, F.W. McLafferty, Infrared multiphoton dissociation of large multiply charged ions for biomolecule sequencing, Anal. Chem. 66 (18) (1994) 2809–2815.
[21] J.A. Madsen, M.W. Gardner, S.I. Smith, A.R. Ledvina, J.J. Coon, J.C. Schwartz, G.C. Stafford Jr., J.S. Brodbelt, Top-down protein fragmentation by infrared multiphoton dissociation in a dual pressure linear ion trap, Anal. Chem. 81 (21) (2009) 8677–8686.
[22] S.A. Raspopov, A. El-Faramawy, B.A. Thomson, K.M. Siu, Infrared multiphoton dissociation in quadrupole time-of-flight mass spectrometry: top-down characterization of proteins, Anal. Chem. 78 (13) (2006) 4572–4577.
[23] F. Lermyte, J.P. Williams, J.M. Brown, E.M. Martin, F. Sobott, Extensive charge reduction and dissociation of intact protein complexes following electron transfer on a quadrupole-ion mobility-time-of-flight MS, J. Am. Soc. Mass Spectrom. 26 (7) (2015) 1068–1076, https://doi.org/10.1007/s13361-015-1124-z.
[24] J.P. Williams, L.J. Morrison, J.M. Brown, J.S. Beckman, V.G. Voinov, F. Lermyte, Top-down characterisation of denatured proteins and native protein complexes using electron capture dissociation implemented within a modified ion mobility-mass spectrometer, Anal. Chem. (2020), https://doi.org/10.1021/acs.analchem.9b04763.
[25] L.J. Morrison, J.S. Brodbelt, 193 Nm ultraviolet photodissociation mass spectrometry of tetrameric protein complexes provides insight into quaternary and secondary protein topology, J. Am. Chem. Soc. 138 (34) (2016) 10849–10859, https://doi.org/10.1021/jacs.6b03905.
[26] J.P. O'Brien, W. Li, Y. Zhang, J.S. Brodbelt, Characterization of native protein complexes using ultraviolet photodissociation mass spectrometry, J. Am. Chem. Soc. 136 (37) (2014) 12920–12928, https://doi.org/10.1021/ja505217w.
[27] S.N. Sipe, J.S. Brodbelt, Impact of charge state on 193 Nm ultraviolet photodissociation of protein complexes, Phys. Chem. Chem. Phys. 21 (18) (2019) 9265–9276, https://doi.org/10.1039/C9CP01144G.
[28] S.N. Sipe, J.W. Patrick, A. Laganowsky, J.S. Brodbelt, Enhanced characterization of membrane protein complexes by ultraviolet photodissociation mass spectrometry, Anal. Chem. 92 (1) (2020) 899–907, https://doi.org/10.1021/acs.analchem.9b03689.
[29] M.D.A. Mabud, M.J. Dekrey, R.G. Cooks, Surface-induced dissociation of molecular ions, Int. J. Mass Spectrom. Ion Process. 67 (1985) 285–294.
[30] J. Laskin, J.H. Futrell, Surface-induced dissociation of peptide ions: kinetics and dynamics, J. Am. Soc. Mass Spectrom. 14 (12) (2003) 1340–1347.
[31] R.B. Cole, S. LeMeillour, J.C. Tabet, Surface-induced dissociation of protonated peptides: implications of initial kinetic energy spread, Anal. Chem. 64 (4) (1992) 365–371.
[32] R.A. Chorush, D.P. Little, S.C. Beu, T.D. Wood, F.W. McLafferty, Surface-induced dissociation of multiply-protonated proteins, Anal. Chem. 67 (6) (1995) 1042–1046.
[33] E. Stone, K.J. Gillig, B. Ruotolo, K. Fuhrer, M. Gonin, A. Schultz, D.H. Russell, Surface-induced dissociation on a MALDI-ion mobility-orthogonal time-of-flight mass spectrometer: sequencing peptides from an "in-solution" protein digest, Anal. Chem. 73 (10) (2001) 2233–2238.
[34] SELECT SERIES Cyclic IMS ion mobility mass spectrometer : Waters. https://www.waters.com/waters/en_US/SELECT-SERIES-Cyclic-IMS-ion-mobility-mass-spectrometer/nav.htm?cid=135021297&locale=en_US (accessed Jul 6, 2020).
[35] D.T. Snyder, E. Panczyk, A. Somogyi, D. Kaplan, V.H. Wysocki, Simple and minimally invasive SID devices for native mass spectrometry, Anal. Chem. 92 (16) (2020) 11195–11203, https://doi.org/10.1021/acs.analchem.0c01657.
[36] A.Q. Stiving, Z.L. VanAernum, F. Busch, S.R. Harvey, S.H. Sarni, V.H. Wysocki, Surface-induced dissociation: an effective method for characterization of protein quaternary structure, Anal. Chem. 91 (1) (2019) 190–209, https://doi.org/10.1021/acs.analchem.8b05071.
[37] A.E. Blackwell, E.D. Dodds, V. Bandarian, V.H. Wysocki, Revealing the quaternary structure of a heterogeneous noncovalent protein complex through surface-induced dissociation, Anal. Chem. 83 (8) (2011) 2862–2865.
[38] X. Ma, M. Zhou, V.H. Wysocki, Surface induced dissociation yields quaternary substructure of refractory noncovalent phosphorylase B and glutamate dehydrogenase complexes, J. Am. Soc. Mass Spectrom. 25 (3) (2014) 368–379, https://doi.org/10.1007/s13361-013-0790-y.
[39] V.H. Wysocki, C.M. Jones, A.S. Galhena, A.E. Blackwell, Surface-induced dissociation shows potential to Be more informative than collision-induced dissociation for structural studies of large systems, J. Am. Soc. Mass Spectrom. 19 (7) (2008) 903–913, https://doi.org/10.1016/j.jasms.2008.04.026.
[40] S.R. Harvey, J.T. Seffernick, R.S. Quintyn, Y. Song, Y. Ju, J. Yan, A.N. Sahasrabuddhe, A. Norris, M. Zhou, E.J. Behrman, S. Lindert, V.H. Wysocki, Relative interfacial cleavage energetics of protein complexes revealed by

surface collisions, Proc. Natl. Acad. Sci. U.S.A. 116 (17) (2019) 8143–8148, https://doi.org/10.1073/pnas.1817632116.
[41] R.S. Quintyn, J. Yan, V.H. Wysocki, Surface-induced dissociation of homotetramers with D2 symmetry yields their assembly pathways and characterizes the effect of ligand binding, Chem. Biol. 22 (5) (2015) 583–592, https://doi.org/10.1016/j.chembiol.2015.03.019.
[42] F. Busch, Z.L. VanAernum, Y. Ju, J. Yan, J.D. Gilbert, R.S. Quintyn, M. Bern, V.H. Wysocki, Localization of protein complex bound ligands by surface-induced dissociation high-resolution mass spectrometry, Anal. Chem. 90 (21) (2018) 12796–12801, https://doi.org/10.1021/acs.analchem.8b03263.
[43] Y. Song, M.T. Nelp, V. Bandarian, V.H. Wysocki, Refining the structural model of a heterohexameric protein complex: surface induced dissociation and ion mobility provide key connectivity and topology information, ACS Cent. Sci. 1 (9) (2015) 477–487, https://doi.org/10.1021/acscentsci.5b00251.
[44] C.A. Romano, M. Zhou, Y. Song, V.H. Wysocki, A.C. Dohnalkova, L. Kovarik, L. Paša-Tolić, B.M. Tebo, Biogenic manganese oxide nanoparticle formation by a multimeric multicopper oxidase mnx, Nat. Commun. 8 (1) (2017) 1–8, https://doi.org/10.1038/s41467-017-00896-8.
[45] Tunable Hetero-Assembly of a Plant Pseudoenzyme-Enzyme Complex, bioRxiv, 2019. https://www.biorxiv.org/content/10.1101/717082v2 (accessed Jul 6, 2020).
[46] J.C. Schwartz, A.P. Wade, C.G. Enke, R.G. Cooks, Systematic delineation of scan modes in multidimensional mass spectrometry, Anal. Chem. 62 (17) (1990) 1809–1818.
[47] J. Gault, M. Liko, D. Landreh, D. Shutin, J.R. Bolla, D. Jefferies, M. Agasid, H.-Y. Yen, M.J.G.W. Ladds, D.P. Lane, S. Khalid, C. Mullen, P. Remes, R. Huguet, G. McAlister, M. Goodwin, R. Viner, J. Syka, C.V. Robinson, Combining 'native' with 'omics' based mass spectrometry to identify endogenous ligands bound to membrane proteins, Nat. Methods 17 (2020) 505–508, https://doi.org/10.1038/s41592-020-0821-0.
[48] K. Håkansson, M.J. Chalmers, J.P. Quinn, M.A. McFarland, C.L. Hendrickson, A.G. Marshall, Combined electron capture and infrared multiphoton dissociation for multistage MS/MS in a fourier transform ion cyclotron resonance mass spectrometer, Anal. Chem. 75 (13) (2003) 3256–3262, https://doi.org/10.1021/ac030015q.
[49] J.J. Coon, B. Ueberheide, J.E. Syka, D.D. Dryhurst, J. Ausio, J. Shabanowitz, D.F. Hunt, Protein identification using sequential ion/ion reactions and tandem mass spectrometry, Proc. Natl. Acad. Sci. Unit. States Am. 102 (27) (2005) 9463–9468.
[50] D.M. Horn, Y. Ge, F.W. McLafferty, Activated ion electron capture dissociation for mass spectral sequencing of larger (42 KDa) proteins, Anal. Chem. 72 (20) (2000) 4778–4784.
[51] D.L. Swaney, G.C. McAlister, M. Wirtala, J.C. Schwartz, J.E. Syka, J.J. Coon, Supplemental activation method for high-efficiency electron-transfer dissociation of doubly protonated peptide precursors, Anal. Chem. 79 (2) (2007) 477–485.
[52] A.R. Ledvina, G.C. McAlister, M.W. Gardner, S.I. Smith, J.A. Madsen, J.C. Schwartz, G.C. Stafford Jr., J.E. Syka, J.S. Brodbelt, J.J. Coon, Infrared photoactivation reduces peptide folding and hydrogen-atom migration following ETD tandem mass spectrometry, Angew. Chem. Int. Ed. 48 (45) (2009) 8526–8528.
[53] N.M. Riley, M.S. Westphall, J.J. Coon, Sequencing larger intact proteins (30-70 KDa) with activated ion electron transfer dissociation, J. Am. Soc. Mass Spectrom. 29 (1) (2017) 140–149.
[54] C.K. Frese, A.M. Altelaar, H. van den Toorn, D. Nolting, J. Griep-Raming, A.J. Heck, S. Mohammed, Toward full peptide sequence coverage by dual fragmentation combining electron-transfer and higher-energy collision dissociation tandem mass spectrometry, Anal. Chem. 84 (22) (2012) 9668–9673.
[55] C.M. Crittenden, E.E. Escobar, P.E. Williams, J.D. Sanders, J.S. Brodbelt, Characterization of antigenic oligosaccharides from gram-negative bacteria via activated electron photodetachment mass spectrometry, Anal. Chem. 91 (7) (2019) 4672–4679, https://doi.org/10.1021/acs.analchem.9b00048.
[56] M.E. Belov, E. Damoc, E. Denisov, P.D. Compton, S. Horning, A.A. Makarov, N.L. Kelleher, From protein complexes to subunit backbone fragments: a multi-stage approach to native mass spectrometry, Anal. Chem. 85 (23) (2013) 11163–11173, https://doi.org/10.1021/ac4029328.
[57] C.M. Crittenden, C.M. Herrera, P.E. Williams, D.P. Ricci, L.R. Swem, M.S. Trent, J.S. Brodbelt, Mapping phosphate modifications of substituted lipid A via a targeted MS3 CID/UVPD strategy, Analyst 143 (13) (2018) 3091–3099, https://doi.org/10.1039/C8AN00561C.
[58] M.R. Mehaffey, J.D. Sanders, D.D. Holden, C.L. Nilsson, J.S. Brodbelt, Multistage ultraviolet photodissociation mass spectrometry to characterize single amino acid variants of human mitochondrial BCAT2, Anal. Chem. 90 (16) (2018) 9904–9911, https://doi.org/10.1021/acs.analchem.8b02099.
[59] G. Ben-Nissan, M.E. Belov, D. Morgenstern, Y. Levin, O. Dym, G. Arkind, C. Lipson, A.A. Makarov, M. Sharon, Triple-stage mass spectrometry unravels the heterogeneity of an endogenous protein complex, Anal. Chem. 89 (8) (2017) 4708–4715, https://doi.org/10.1021/acs.analchem.7b00518.
[60] R.S. Quintyn, S.R. Harvey, V.H. Wysocki, Illustration of SID-IM-SID (Surface-Induced dissociation-ion mobility-SID) mass spectrometry: Homo and hetero model protein complexes, Analyst 140 (20) (2015) 7012–7019, https://doi.org/10.1039/C5AN01095K.
[61] R.M. McCarty, V. Bandarian, Deciphering deazapurine biosynthesis: pathway for pyrrolopyrimidine nucleosides toyocamycin and sangivamycin, Chem. Biol. 15 (8) (2008) 790–798, https://doi.org/10.1016/j.chembiol.2008.07.012.
[62] D.T. Snyder, E. Panczyk, A.Q. Stiving, J.D. Gilbert, A. Somogyi, D. Kaplan, V. Wysocki, Design and performance of a second-generation surface-induced dissociation cell for fourier transform ion cyclotron resonance mass spectrometry of native protein complexes, Anal. Chem. 91 (21) (2019) 14049–14057, https://doi.org/10.1021/acs.analchem.9b03746.
[63] M. Zhou, S. Dagan, V.H. Wysocki, Impact of charge state on gas-phase behaviors of noncovalent protein complexes in collision induced dissociation and surface induced dissociation, Analyst 138 (5) (2013) 1353–1362, https://doi.org/10.1039/c2an36525a.
[64] K. Pagel, S.-J. Hyung, B.T. Ruotolo, C.V. Robinson, Alternate dissociation pathways identified in charge-reduced protein complex ions, Anal. Chem. 82 (12) (2010) 5363–5372, https://doi.org/10.1021/ac101121r.
[65] R.S. Quintyn, M. Zhou, J. Yan, V.H. Wysocki, Surface-induced dissociation mass spectra as a tool for distinguishing different structural forms of gas-phase multimeric protein complexes, Anal. Chem. 87 (23) (2015) 11879–11886.
[66] C.M. Jones, R.L. Beardsley, A.S. Galhena, S. Dagan, G. Cheng, V.H. Wysocki, Symmetrical gas-phase dissociation of noncovalent protein complexes via surface collisions, J. Am. Chem. Soc. 128 (47) (2006) 15044–15045, https://doi.org/10.1021/ja064586m.
[67] A.S. Galhena, S. Dagan, C.M. Jones, R.L. Beardsley, V.H. Wysocki, Surface-induced dissociation of peptides and protein complexes in a quadrupole/time-of-flight mass spectrometer, Anal. Chem. 80 (5) (2008) 1425–1436, https://doi.org/10.1021/ac701782q.
[68] M. Zhou, Incorporation of Surface Induced Dissociation into a Commercial Ion Mobility – Tandem Mass Spectrometer and Application of Mass Spectrometry Methods for Structural Analysis of Non-covalent Protein Complexes, Dissertation, The Ohio State University, The Ohio State University, 2013.
[69] Z.L. VanAernum, J.D. Gilbert, M.E. Belov, A.A. Makarov, S.R. Horning, V.H. Wysocki, Surface-induced dissociation of noncovalent protein complexes in an extended mass range Orbitrap mass spectrometer, Anal. Chem. 91 (5) (2019) 3611–3618, https://doi.org/10.1021/acs.analchem.8b05605.
[70] J. Yan, M. Zhou, J.D. Gilbert, J.J. Wolff, A. Somogyi, R.E. Pedder, R.S. Quintyn, L.J. Morrison, M.L. Easterling, L. Pasa-Tolic, V.H. Wysocki, Surface-induced dissociation of protein complexes in a hybrid fourier transform ion cyclotron resonance mass spectrometer, Anal. Chem. 89 (1) (2017) 895–901, https://doi.org/10.1021/acs.analchem.6b03986.
[71] R. Wörgötter, J. Kubišta, J. Žabka, Z. Dolejšek, T. Märk, Z. Herman, Surface-induced reactions and decomposition of the benzene molecular ion C6H6+: product ion intensities, angular and translational energy distributions, Int. J. Mass Spectrom. Ion Process. 174 (1–3) (1998) 53–62.
[72] H.L. de Clercq, A.D. Sen, A.K. Shukla, J.H. Futrell, Inelastic ion-surface collisions: scattering and dissociation of low energy benzene molecular cations, Int. J. Mass Spectrom. 212 (1–3) (2001) 491–504.
[73] M. Meot-Ner, A.R. Dongre, A. Somogyi, V.H. Wysocki, Thermal decomposition kinetics of protonated peptides and peptide dimers, and comparison with surface-induced dissociation, Rapid Commun. Mass Spectrom. 9 (9) (1995) 829–836, https://doi.org/10.1002/rcm.1290090922.
[74] J. Laskin, Energetics and dynamics of fragmentation of protonated leucine enkephalin from time- and energy-resolved surface-induced dissociation studies, J. Phys. Chem. 110 (27) (2006) 8554–8562, https://doi.org/10.1021/jp057229r.
[75] M.T. Donor, A.M. Mroz, J.S. Prell, Experimental and theoretical investigation of overall energy deposition in surface-induced unfolding of protein ions, Chem. Sci. 10 (14) (2019) 4097–4106, https://doi.org/10.1039/C9SC00644C.
[76] A.J. Wirth, Y. Liu, M.B. Prigozhin, K. Schulten, M. Gruebele, Comparing fast pressure jump and temperature jump protein folding experiments and simulations, J. Am. Chem. Soc. 137 (22) (2015) 7152–7159, https://doi.org/10.1021/jacs.5b02474.
[77] Y. Song, Protein Primary and Quaternary Structure Elucidation by Mass Spectrometry, The Ohio State University, 2015.
[78] M. Zhou, S. Dagan, V.H. Wysocki, Protein subunits released by surface collisions of noncovalent complexes: nativelike compact structures revealed by ion mobility mass spectrometry, Angew. Chem. Int. Ed. 51 (18) (2012) 4336–4339.
[79] D. Schultz, H. Lim, S. Garbis, L. Hanley, Energy partitioning in the surface-induced dissociation of linear and cyclic protonated peptides at an organic surface, J. Mass Spectrom. 34 (3) (1999) 217–225.
[80] J. Wang, S.O. Meroueh, Y. Wang, W.L. Hase, Efficiency of energy transfer in protonated diglycine and dialanine SID: effects of collision angle, peptide ion size, and intramolecular potential, Int. J. Mass Spectrom. 230 (1) (2003) 57–63.
[81] H. Lim, D.G. Schultz, E.A. Gislason, L. Hanley, Activation energies for the fragmentation of thiophene ions by surface-induced dissociation, J. Phys. Chem. B 102 (23) (1998) 4573–4580.
[82] J. Laskin, T.H. Bailey, J.H. Futrell, Shattering of peptide ions on self-assembled monolayer surfaces, J. Am. Chem. Soc. 125 (6) (2003) 1625–1632, https://doi.org/10.1021/ja027915t.
[83] J. Laskin, T.H. Bailey, J.H. Futrell, Mechanisms of peptide fragmentation from time-and energy-resolved surface-induced dissociation studies: dissociation of angiotensin analogs, Int. J. Mass Spectrom. 249 (2006) 462–472.
[84] S.O. Meroueh, Y. Wang, W.L. Hase, Direct dynamics simulations of collision- and surface-induced dissociation of N-protonated Glycine. Shattering fragmentation, J. Phys. Chem. 106 (42) (2002) 9983–9992.
[85] K. Park, B. Deb, K. Song, W.L. Hase, Importance of shattering fragmentation in

the surface-induced dissociation of protonated octaglycine, J. Am. Soc. Mass Spectrom. 20 (6) (2009) 939–948, https://doi.org/10.1016/j.jasms.2009.02.028.

[86] G.L. Barnes, A. Shlaferman, M. Strain, Fast fragmentation during surface-induced dissociation: an examination of peptide size and structure, Chem. Phys. Lett. 754 (2020) 137716, https://doi.org/10.1016/j.cplett.2020.137716.